Reconstructing Electrospray Plume Current Spatial Distributions using Computed Tomography

IEPC-2019-A-787

Presented at the 36th International Electric Propulsion Conference
University of Vienna, Austria
September 15-20, 2019

Daniel G. Courtney*, Zackary Wood† and Timothy Fedkiw‡
Busek Co., Natick, MA, 01720, USA

Electrospray thruster designs generally encompass a degree of physical multiplexing to achieve desired thrust levels. Aggregate total beam currents and mass-flow rates can be measured directly yet do not provide an assessment of the current sharing between structures. Here computed tomography techniques are applied to reconstruct the spatial distribution of the plume current emitted from an electrospray thruster. Reconstructions are derived from current measurements obtained using a custom-made instrument designed to sweep a thin wire radially across the plume at numerous controlled angles with respect to horizontal. This approach results in a low degree of plume interception by the instrument ($\sim 1\%$ or less) and ensures that all such-interception contributes to the measurement. To assess the viability and limitations of this approach, simulations of the reconstruction are presented using calculated notional plume maps. Example data obtained using a Busek BET-300-P electrospray thruster are presented at current levels from $0.2\mu A$ up to $600\mu A$. At sub-μA currents, discrete concentrations of current were observed and, through corroboration via far-field plume profiles, attributed to individual (or tightly packed) emission sites. Sample reconstructions obtained while accruing a high level of throughput ($\mathbf{31}Ns$) are presented and indicate a significant transition in emission localization over time. Results are discussed in the context of understanding the make-up of BET-300-P far-field plume profiles and in assessing the low-thrust control capabilities of highly multiplexed passive electrospray thrusters.

Nomenclature

Δr	= radial position step size (mm)
ϕ	= probe angle with respect to horizontal
$h(r)$	= apodized ramp filter
I	= Collected current (μA)
j	= Current density ($\mu A/mm^2$)
L	= probe length (mm)
N_ϕ	= number of measurement angles
N_r	= number of radial positions
$p_\phi(r)$	= filtered sinogram data (μA)
r	= radial probe position (mm)
W	= probe width (mm)
Z_{probe}	= axial distance from emission sources to probe wire (mm)

*Chief Scientist, Micro-Propulsion Group, dcourtney@busek.com.
†Research Engineer, Micro-Propulsion Group, zwood@busek.com.
‡Research Engineer, Micro-Propulsion Group, tpfedkiw@busek.com.

I. Introduction

Electrospray propulsion systems -including colloidal and relatively ionic sources from metal and non-metal propellants inherently include a degree of emission multiplexing[1–6] to augment thrust output. In most applications this manifests as an array -from less than ten to many hundred- of emitter structures operated in parallel. As electrical current serves as the prime -if not only- means of measuring instantaneous mass flow rate, a parallel arrangement does not implicitly permit measurement of current or flow sharing between emitters. Inefficient current sharing -where some emitters or emission regions provide a disproportioned fraction of the total current- may accelerate localized degradation and thereby limit the overall thruster life; for example, via an intolerable degree of primary beam interception by grid electrodes.[7]

Electrospray current spatial distribution measurement techniques have previously included use of ablation plates[8,9] and rastered point probes.[10] Ablation plates necessarily lead to a significant degree of emitter to plate interaction wherein sputtered material can quickly degrade output and thereby the fidelity of the result with respect to normal operation.[9] Rastered probes, where a small point of current-collecting surface is moved across the face of the thruster can provide a significant improvement in this regard. However; significant impinged structure remains in the probe hardware and associated insulating elements necessary to limit current collection to a small point. As an alternative we have applied a computed tomography method which reconstructs a map of current from line integrated currents along a wire. This method seeks to reduce interference with the source. The importance of reducing sources of degrading interference cannot be understated given that the improvement and study of electrospray thruster lifetime remains a central topic for development. Accordingly, current maps acquired periodically over extended durations of operation are desirable and necessitate minimally invasive techniques.

Computed tomography techniques have been applied previously in the study of plasma sources including spacecraft thrusters.[11–15] In numerous instances, a presumption of an axisymmetric plume has enabled use of Abel inversions or other similar but noise-optimized approaches. Reconstructions of all kinds and particularly those without an axisymmetric assumption have predominantly been achieved using optical methods; including investigations into arcject performance.[12] However; in for example, Ref [15], a wire was swept through the plume of a Hall-Thruster -in addition to optical measurements- when applying an axisymmetric reconstruction technique. Plumes originating from multiplexed electrospray or LMIS arrays are not, typically, axisymmetric. Moreover, the low-density plumes of particles emitted from electrospray thrusters generate a weak optical signature which may not inherently be proportional to current density. A wire-probe based approach which does not assume symmetry was therefore desired.

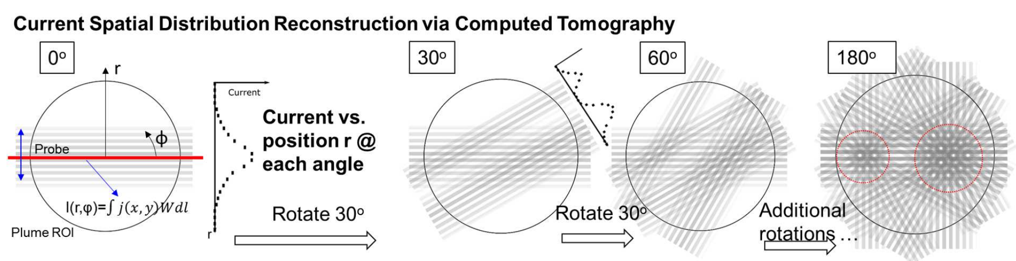

Figure 1. Simplified overview of the scanning-wire based computed tomography technique applied to map electrospray plumes in the presented work.

Referring to Figure 1, the current collected by a thin wire strung across the thruster plume equates to the integration of current density $j(x, y)$ times width W along the wire length. In an axisymmetric approach an estimate of the distribution can be achieved by sweeping the probe linearly through the plume at one angle. In contrast, multiple probe sweeps are performed at defined angles here. The assembly of these data, over all positions and at angles between 0^o and 180^o constitutes a discrete estimate of the Radon transform of the current density.[16] Numerous methods exist to invert the Radon transform to yield the current density j(x,y), see for example the overviews in Refs. [11, 16, 17]. These methods form the basis of computed tomography techniques widely developed for medical and other imaging applications. Figure 1 visualizes how the data obtained can yield a 2D current map. Measurements projected back onto a cartesian plane can be summed at each angle, leading to an image. Immediate backprojection of raw data as depicted in the schematic does not, mathematically, yield a high fidelity reconstruction. Instead filtration is required to appropriately and accurately apply this backprojection technique.

This manuscript emphasizes the instrument design and analytical approach along with measures taken to verify if the technique can provide useful data in the context of electrospray plumes. In support of such verification, reconstructions of calculated (idealized) thruster plumes were performed by simulating the CT experiment. A Busek BET-300-P[18] thruster was then operated at a sufficiently low current to generate and probe only a few emission sites. Additional sample data are provided at increasing current levels and over long durations of operation. Finally, discussions comparing simulated and observed plumes are provided along with preliminary interpretations of the acquired data in the broader context of enhancing the understanding of passive electrospray thrusters.

II. Apparatus, Methodology and Simulation Results

A. Experimental Apparatus

Figure 2 presents Busek's computed tomography instrument as viewed from the up- and down-stream orientations. A $50\mu m$ tungsten wire constitutes the probe. This wire is mounted on a precision linear translation stage used to sweep the wire through +/- 24mm about the instrument centre. The linear translation stage is itself mounted on a custom-made, low-profile rotation stage providing $> 180^o$ of motion. The instrument has been designed such that when the probe wire is positioned a few mm from the thruster face, no structural elements are within 55^o of the plume; greater than the $\sim 45^o$ plume half-angle previously reported from electrospray thrusters similar to those tested here.[4] In this manner, only the small area of current collecting surface along the wire is impinged by the beam. The probe current was measured with a Keithley 6485 picoammeter.

Secondary charge interactions between the probe wire and thruster are suppressed via a potential bias. In the majority of data presented here the thruster extractor electrode, located in close proximity to the probe wire, was held at a high negative potential (approximately $-100V$) in order to suppress ion-induced electron currents from leaving the probe wire. This arrangement differs from that which may be more applicable in a plasma plume, where the probe wire may be biased to a negative value with respect to the plasma in order to repel the local electron population. As free-electrons are not implicitly generated from electrospray thrusters, suppression of ion-induced electron emission is typically favoured. However; the validity of this assumption in the context of the presented work requires further review in later efforts.

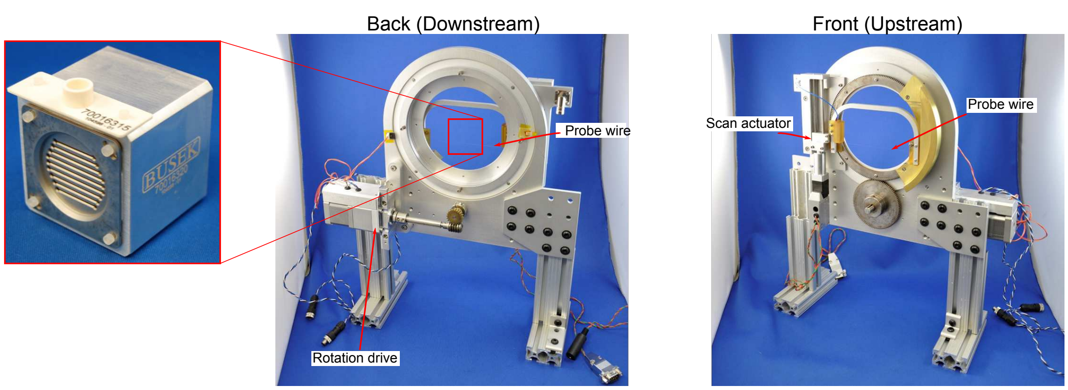

Figure 2. Wire-probe based computed tomography current mapping instrument and Busek's BET-300-P passively fed electrospray thruster.

Several limitations in the prototype instrument design and assembly have been identified: i) significant backlash in angle position, ii) an angle-dependent slop in radial position and, iii) slow radial position feedback. Effects due to backlash in the angular stage are avoided by operating in a single direction beginning from a hardware defined home position. Angle-dependent slop refers to a slight twist in the probe mount when the direction of torque due to the probe mass changes with respect to the direction of positive motor travel between 0^o and 180^o. To compensate for this shift in true probe position, the centre radial position was measured over the full angular range (0^o to 180^o) facilitating formulation of an angle dependent correction factor. However; as shown in the results below, evidence of continued position variability depending on the travel direction remained at some angles. In future hardware iterations this issue may be corrected through mechanical improvements to the stage design. Finally, radial position readouts are limited by the maximum response rate of the linear actuator (25 Hz), at a sweep rate of 4 mm/s, which is otherwise sustainable by the actuator, this corresponds to a positional data rate of one sample per $0.16mm$; or only 300 samples over the 48 mm range to be probed. To improve this rate, the measured current data are sampled at a higher rate (typically 100 Hz) and the position is linearly interpolated between actual readouts. A correction is made to account for the finite polling and response processing time inherent to the stage.

Several Busek BET-300-P electrospray thrusters were used in collecting the presented experimental results. The thrusters were operated using bench-top supplies using a configuration similar to that described in Ref. [18]. Current-control was achieved using software-based feedback of the current measured by Busek's custom-made inline current monitors. The BET-300-P is a passively fed thruster with a nominal thrust range of $0\mu N$ to $\sim 150\mu N$ corresponding to a maximum current of up to $800\mu A$. Figure 2 includes an image of a BET-300-P. In addition to the near-field CT measurements, far-field current maps were recorded using a Kimball Physics FC-72 Faraday cup with $11.28mm$ aperture mounted on a rotating arm at a radial distance of 49 cm from the thruster face. The axis of probe rotation was perpendicular to the emitter edges. As discussed below, rotation about an axis parallel to the emitter edges may have provided more informative data and will be pursued in the future. All measurements were performed in Busek's T16 facility with a base pressure of $\sim 5x10^{-7}Torr$ and a typical operating pressure $< 1.0x10^{-5}Torr$.

B. Analysis Methodology

As described in the introduction, raw data obtained using the instrument comprise measured currents over an array of N_r probe radial positions and N_ϕ angles. Referring to equation 1, each measurement corresponds to the line integrated current density $j(r,\phi)$ along the probe length L, and width W. In practice, data are obtained continuously in time. For each of the N_r discrete radial positions measured, current data obtained within $\pm\Delta r/2$ are averaged to generate the discrete matrix. The resultant matrix $I(r,\phi)$ forms a sinogram, see Figure 3(c) below, which is a discrete estimate of the Radon transform of the current per unit of wire length.[16] These data are then analyzed using a filtered backprojection algorithm developed from well defined computed tomography theory and methods discussed at length in the literature.[11,16,17] The selected filtering approach follows the recommendations outlined in section 3.3.3 of Ref [17] summarized in equation 2 (equation 69 in the reference). Here $p_\phi(r)$ are the filtered sinogram data generated for each raw data vector corresponding to a measurement angle ϕ. The data are filtered using a bandlimited ramp filter $h(r)$. As recommended by the reference, a bandlimited ramp filter has been generated by discrete sampling at the same spatial interval as the measured data, Δr. After zero-padding, the algorithm convolutes the ramp filter with the measured data. Finally, the data are smoothed using a Shepp-Logan filter then transformed back to the spatial (radial position) domain in advance of the backprojection process.

$$I(r,\phi) = \int_L j(x,y)W dl \tag{1}$$

$$p_\phi(r) = \Delta r \left[IFFT\left[\text{FFT of } I(r,\phi)\right]\left[\text{FFT of } h(r)\right]\left[Shepp - Logan\right]\right] \tag{2}$$

Pixel-driven backprojection using linear radial interpolation has been employed to reconstruct the current distribution. Equation 3 summarizes the operation, including normalization by the probe width W to obtain the current density $j(x,y)$ with units A/mm^2. To estimate $p_\phi(r_{px})$, the filtered data at the centre of each pixel (where $r = r_{px}$), the measured data are linearly interpolated as in equation 4. Specifically, contributions due to the two radial measurements positions nearest to each pixel centre are scaled based on each measurement's radial distance from the pixel centre. These contributions are then summed. In the expressions below, tri(t) is defined as being equal to $1 - |t|$ for $|t| < 1$ and zero otherwise. Details of this procedure are outlined in, for example, Ref [16].

$$j\left(x,y\right) \approx \frac{\pi}{WN_\phi}\sum_{i=1}^{N_\phi} p_\phi\left(r_{px}\right) \tag{3}$$

$$p_\phi(r_{px}) \approx \sum_{N_r} p_\phi(r)\text{tri}\frac{r_{px} - r(n)}{\Delta r} \tag{4}$$

C. Simulated Experiments

Prior to developing a physical probe, CT reconstruction experiments were simulated numerically in order to establish viability of the technique/algorithm and gain an appreciation for the expected results. Simulations comprised developing a randomized map of emission site locations spread over the nine Busek BET-300-P emitter edges. Each emission site was assumed to emit an equal, user-defined, level of current normally distributed over emission angle with a plume width based on empirical data. The emission site localization map (Figure 3(a)) was then applied to simulate both the nominal current distribution and the result obtained via CT reconstruction. The nominal map corresponds to the cumulative calculated current at each point on a two dimensional grid positioned a fixed axial distance Z_{probe} from the emission plane.

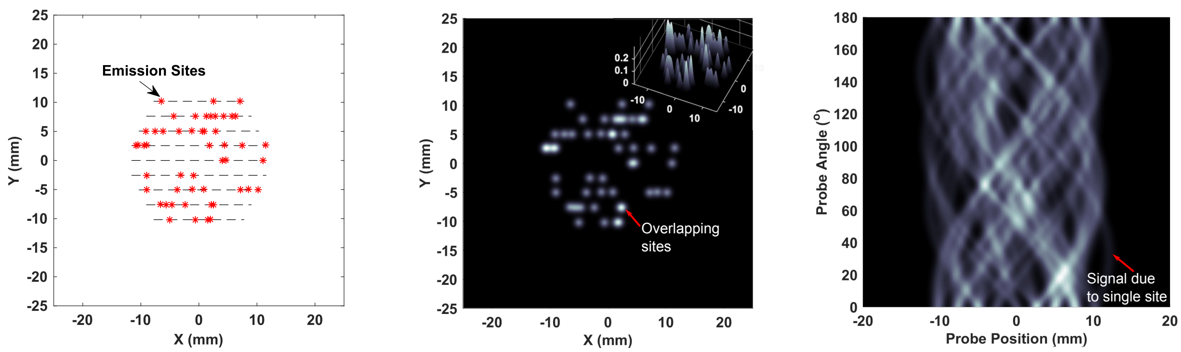

(a) (b) (c)

Figure 3. A) Simulated emission site locations, B) Simulated current map at $Z_{probe} = 4mm$, C) Simulated sinogram (instrument data) at at $Z_{probe} = 4mm$.

Figure 3(b) presents the nominal (not reconstructed) distribution when emitting $12.5\mu A$ of total current from each of the 50 emission sites in Fig. 3(a). Each site was assumed to provide $0.25\mu A$ of total current and to have a Gaussian width (one standard deviation) of 8^o; consistent with far-field plume maps of the BET-300-P thruster obtained at Busek. The CT experiment was then simulated by calculating the cumulative current at each point along a discrete simulation of the probe wire; these values were then integrated as in equation 1 to yield a simulated sinogram, see Figure 3(c). Finally, the simulated data are were input to the analysis algorithm described above in the same manner as to be performed with experimental data; yielding an estimate of the current map after reconstruction.

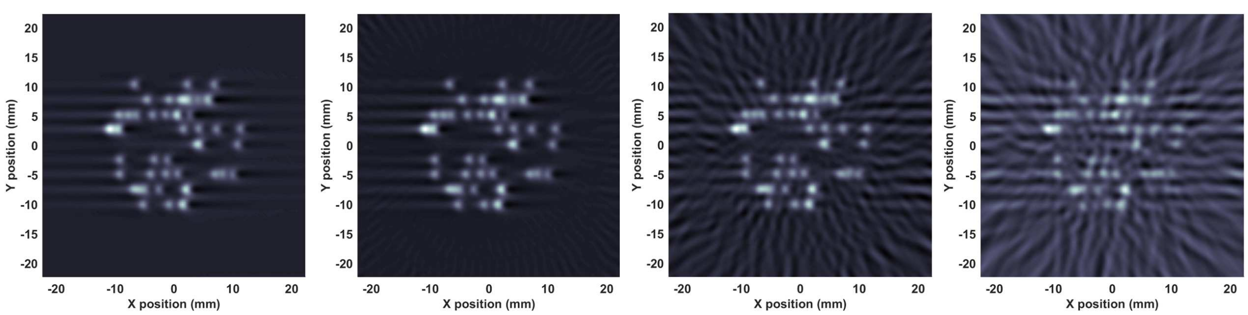

(a) $N_\phi = 120$ (b) $N_\phi = 60$ (c) $N_\phi = 30$ (d) $N_\phi = 15$

Figure 4. Simulated CT reconstructions using the indicated number of angles and $N_r = 121$ steps in all cases. Significant artifacts are visible as N_ϕ reduces below N_r.

Referring to Ref [16], the number of angular sample positions N_ϕ should be at least $N_r\pi/2$ to ensure spacings between points at high radial position in the angular direction are comparable to the period along the radial axis. However; while use of N_ϕ significantly less than N_r reduces the resolution and fidelity of the reconstruction it also reduces the total experiment time required to obtain an image. The examples in Figure 4 demonstrate reconstructed plume maps obtained at the indicated N_ϕ while maintaining $N_r = 121$. Referring to Figure 4(a) (when $N_\phi = 120$, the method supports a high fidelity reconstruction of the original/expected current map (Fig. 3(b)). However; increasingly significant artifacts and degraded resolution are evident as the number of angles is reduced compared with the number of radial positions. Despite these artifacts, that the broad distribution of sites (for example that no emission is present in the bottom right corner of the thruster face) is retained with only $N_\phi = 30$ is practically significant within the context of minimizing measurement time and thereby plume interference.

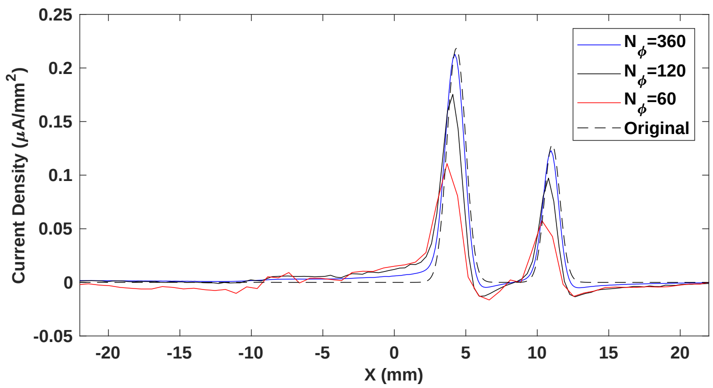

Figure 5. Reduced sampling resolution contributes to a reduction in quantitative agreement with the simulated plume.

Quantitatively, point by point agreement with the nominal current map is highly dependent on the measurement resolution. Figure 5 demonstrates a section of data through the centre of the plume where $Y = 0$ for the same random emission site map sampled above; again considering a plane $4mm$ from the emission sites. Three curves are shown corresponding to N_ϕ equal to 360, 120 and 60 angles; the number of radial positions N_r was equal to $N_\phi + 1$ in all cases. Referring to the blue and dashed curves, when $N_\phi = 360$ the current density at each point as calculated by the CT reconstruction is in good agreement with the original distribution. However; as the number of angles sampled and therefore resolution was decreased this agreement was no longer maintained. This result is not unexpected given the high spatial frequencies inherent. Specifically, as the spatial sampling period becomes comparable with the feature width (the width of each emission plume), the CT reconstruction smoothes out the image and therefore point-to-point quantitative comparisons are no longer appropriate. It is noteworthy, however that for all cases the total integrated current agreed with the actual output ($12.5\mu A$) to within less than 5%. This largely qualitative discussion requires significant further review in the context of ensuring stability in the reconstruction results despite the high spatial frequencies inherent to these plumes.

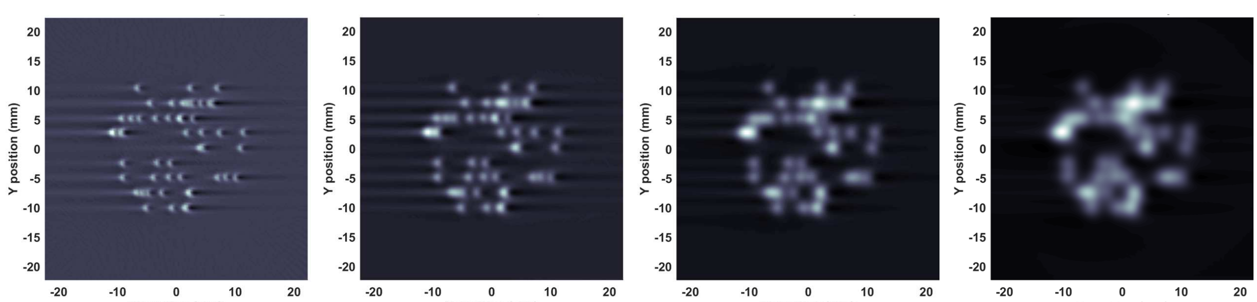

(a) $Z_{probe} = 2mm$ (b) $Z_{probe} = 4mm$ (c) $Z_{probe} = 6mm$ (d) $Z_{probe} = 8mm$

Figure 6. Simulated CT reconstructions at the indicated Z_{probe} with $N_\phi = 120$ and $N_r = 121$ steps in all cases. Significant artifacts are visible as N_ϕ reduces below N_r.

Due to the superposition of adjacent beams, the degree to which this method can accurately pinpoint emission localization is strongly dependent on the distance from the sources to the wire probe, Z_{probe}. In Figure 6, simulations are made, using the same test pattern shown in Figure 4 with the wire probe positioned at $2mm$ increments from $Z_{probe} = 2mm$ to $Z_{probe} = 8mm$. Here $N_\phi = 120$ and $N_r = 121$ in all cases. At between 6 mm and 8 mm, utility is expected to be primarily relegated to broad emission localization, as opposed to identification or tracking of individual sites. This issue is expected to be compounded as the number of active emission sites increases.

The presented samples demonstrate the efficacy of the CT reconstruction method when applied to conditions representative of an expected electrospray plume. However; several critical parameters are not considered here. As discussed in section IV below, the possibility for mis-alignment of beamlets from the nominal axis can contribute significantly to the observed data. In addition, a capability to introduce position and amplitude noise during probe measurement simulations has also been developed. However; for the sake of brevity discussion of those results has been omitted here in favour of the experimental data presented below.

III. Experimental Results

A source supporting a single emission site may have most elegantly enabled validation of the presented instrument. However, resource constraints did not permit such a targeted investigation. Instead a BET-300-P thruster was operated at low currents and with the grid mounting structure superficially modified to enable the probe wire to be positioned at $Z_{probe} = 4mm$. The thruster was then commanded to low currents (on the order of a micro-ampere) while measuring both the near-field (with the CT instrument) and far-field (with a Faraday cup) current maps.

Additional sample results using a fully functional BET-300-P are also provided below. During these measurements, the physical design of the BET-300-P necessitated Z_{probe} to be approximately six to eight millimeters. Accordingly (see Fig. 6(d)) a significant reduction in resolution was expected during these measurements.

A. Measurement Repeatability

During these measurements, the radial sweep actuator was configured to operate at 3 mm/s and a complete scan over 120 angles required ∼25 minutes to complete. To be viable, the emission was required to be stable over this time frame (or ideally twice this time frame to sample at the Nyquist limit). To evaluate stability, the probe was swept back and forth over at the same angle (0^o) continuously while maintaining a constant low emission current of $0.4\mu A$. Referring to 7, the data indicate a not-insignificant degree of variation. Specifically in Fig. 7(a), the mean profile over all measurements is plotted along with ± one standard deviation for each position point. Figure 7(b), indicates the RMS deviation between the array of measurements made at a given instant compared with the mean profile. Note that there are several relatively large discontinuities in this metric indicating significant shifts in emission may have occurred; however, over some ∼10 minute periods the RMS deviation is relatively constant. As shown below, images of (presumed) emission sites were well resolved despite this level of variability at low currents.

B. Current Maps at Increasing Commanded Current

Figure 8, was obtained when operating the BET-300-P thruster at 0.2 μA. Here, and for all measurements presented in this section, $N_\phi = 60$ and $N_r = 121$. The left side of the Figure presents the raw sinogram obtained during the measurement. The sinogram clearly features two prominent curves and several less intense signals. Two noteworthy features are evident in the image: i) Discontinuities in the signal curves are visible between ∼60 and ∼100 degrees; this trait has been consistent for all measurements to date and poor localization of the probe stage as the gravity vector dependent torque becomes ambiguous is a leading candidate for the issue. ii) Gaps in data as the angular position was progressed are evident at these low currents, indicating a cessation of collected current inconsistent with the trends. Intermittent emission from a single emission site could, for example, explain this phenomenon. The degree to which this behaviour is due to the low operating currents or present at all levels is significant in assessing the suitability of using this method to probe individual emission site locations.

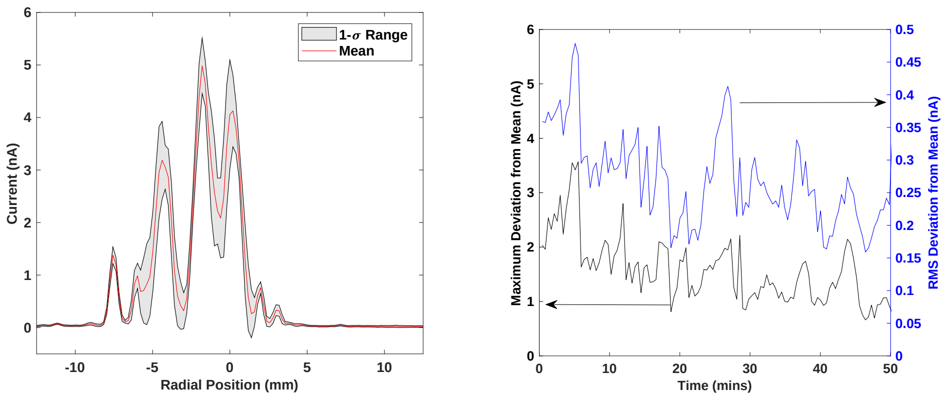

(a) (b)

Figure 7. Variations in radial sweep measurements performed at a single probe angle of zero degrees over a $50min.$ **period.**

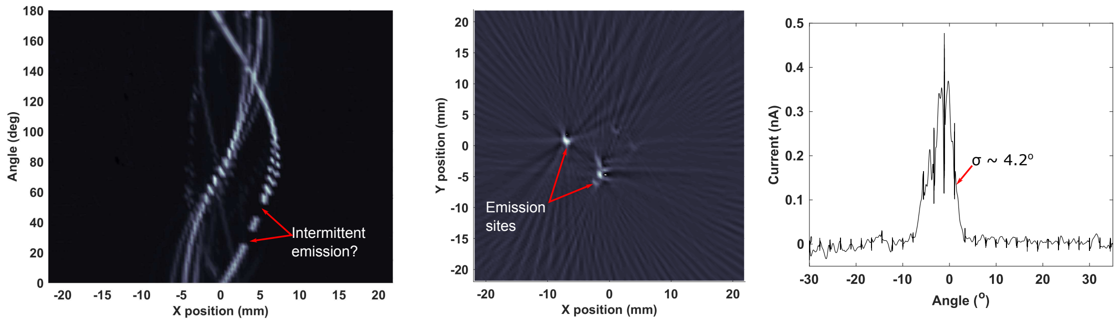

Figure 8. Summary of measurements obtained at $0.2\mu A$ **including the raw (unfiltered) sinogram, reconstructed plume map and far-field plume sweep.**

The central pane of Fig. 8 presents the intensity map obtained via reconstruction. Despite the described issues apparent in the sinogram, two prominent current concentrations flanked by up to four weaker concentrations are resolved. The final (right) pane of the Figure summarizes the far-field plume shape as recorded by the Faraday-cup. The narrow plume angle (4.2^o standard deviation when fit to a Gaussian) observed is noteworthy as being significantly more narrow than the $\sim 7-9^o$ standard deviation more typical of the BET-300-P operating at hundreds of microamps.

Figure 9 summarizes further sets of data obtained at increasing current levels, beginning from $0.4\mu A$ and increasing to $2.0\mu A$. Note that to maximize contrast the image intensity scale has been optimized for each image. As above, at each current, the raw CT probe measurement sinogram is presented along with the reconstructed plume map and one or two (as available) far-field Faraday plume sweeps. Referring to 9(a), the number of current concentrations has increased from four to six at $0.2\mu A$ to nine or ten at $0.4\ \mu A$. Moreover, the far-field plume sweep now reveals three distinct, narrow beamlets spaced between -15^o and $+6^o$. That both the number of current concentrations visible in the reconstructed map and the number of peaks in the far-field sweep increased reinforces the notion that the observed concentrations correspond to individual emission sites or tight clusters thereof.

As the current was increased further, the number of current concentrations (apparent emission sites) also increased. Note that at $1.0\ \mu A$, Figure 9(b), the peak at high negative angle visible at both $0.4\ \mu A$, Fig. 9(a), and $2.0\ \mu A$, Fig. 9(c), is no longer visible. A corresponding disappearance or change in the CT reconstructions was not conclusively identified.

In Figure 10, similar data are presented yet with the beam current further increased to $4.0\mu A$, $10.0\mu A$ and $20.0\ \mu A$ in the three sub-Figures. At these higher currents, the number of current concentrations (emission

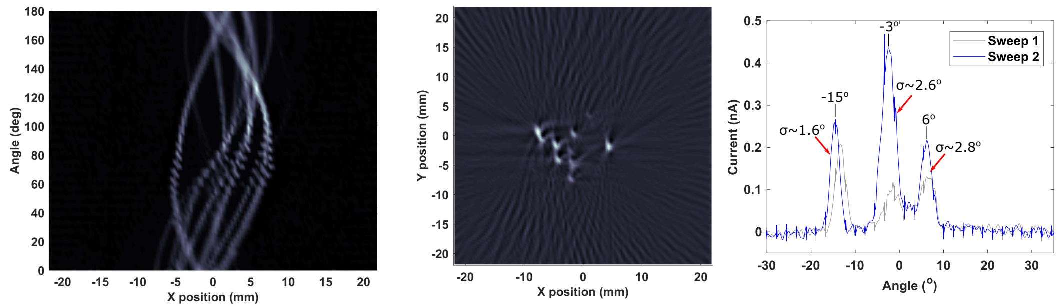

(a) $0.4\mu A$

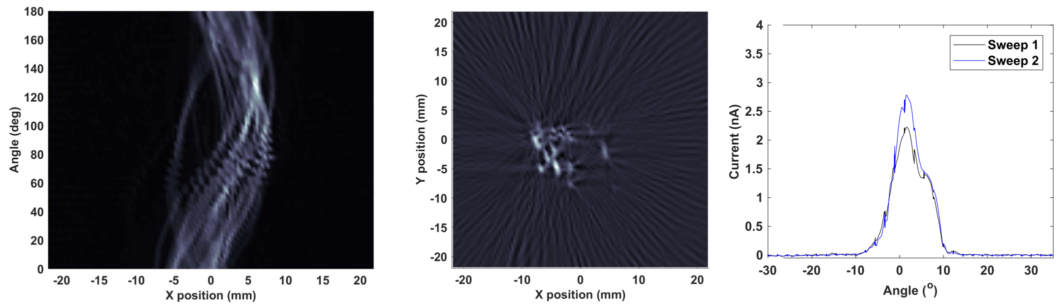

(b) $1.0\mu A$

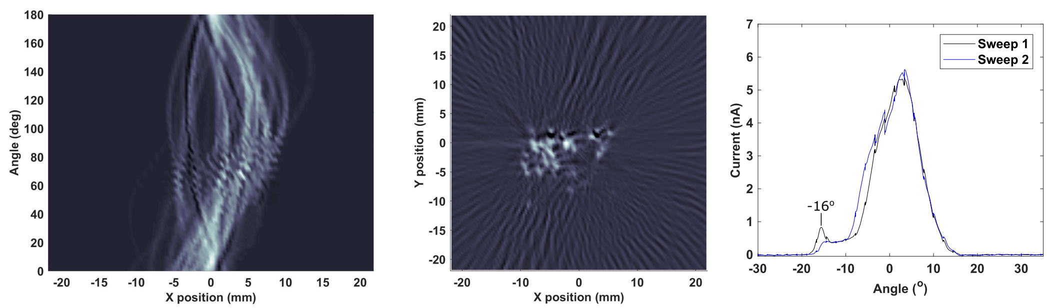

(c) $2.0\mu A$

Figure 9. Summary of measurements obtained at increasing beam current up to $1.0\mu A$, including the raw (unfiltered) sinogram, reconstructed plume map and far-field plume sweep.

sites) is no longer easily estimated and a degree of signal overlap is evident. Nevertheless, an evolution towards a larger activated area is apparent. Despite this increase, clear definition of the nine BET-300-P emission strips cannot be discerned from the images. This is discussed in section IV below.

As beam current is increased, the far-field plume data in Fig. 10 progress toward a relatively centrally located single distribution with a standard deviation of $\sim 9^o$. This evolution from several narrow peaks towards a single plume is significant in interpreting far-field plume map data from the BET-300-P and other similar thrusters in the context of prior measurements made from single electrospray emitters yielding beams with high ion content. Specifically, these data and the increase in emission sites evident via CT reconstructions support the notion that each emission site yields a relatively collimated beam yet the emission axis may vary significantly; largely within 10 or 20 degrees of the axial direction. This concept is discussed further in the next section.

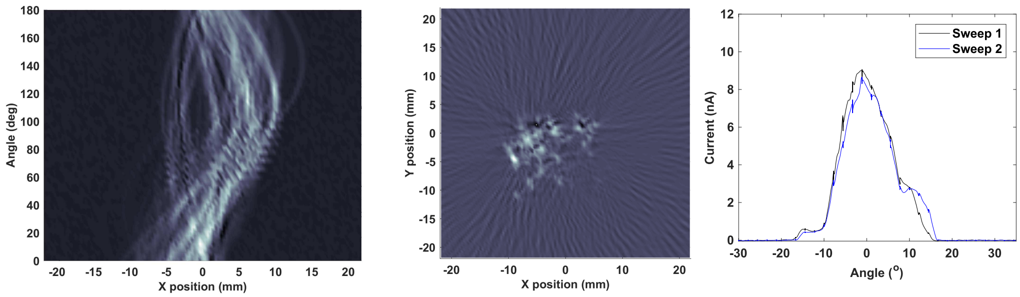

(a) $4.0\mu A$

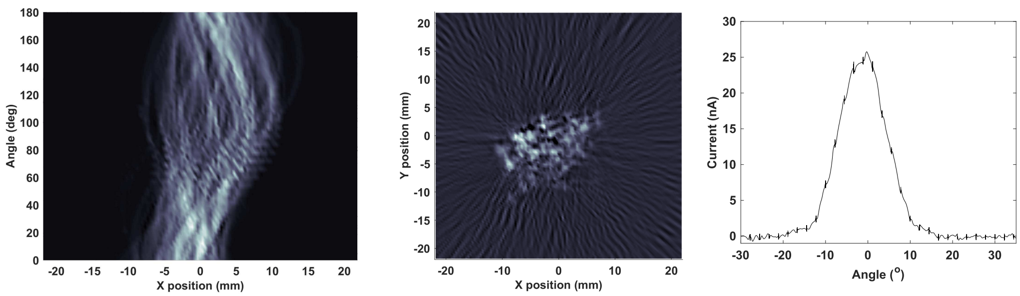

(b) $10.0\mu A$

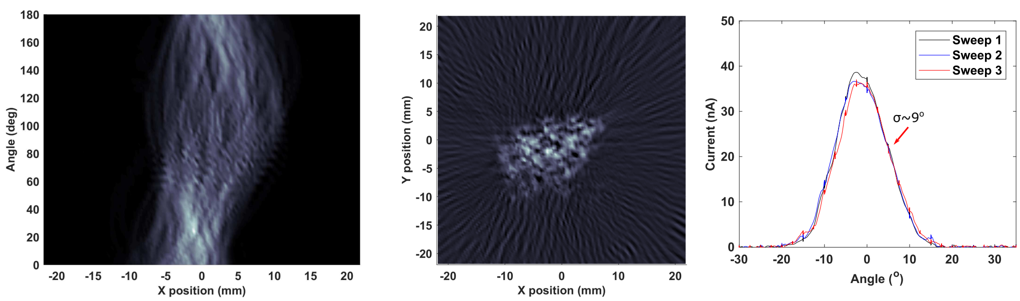

(c) $20.0\mu A$

Figure 10. Summary of measurements obtained at increasing beam current up to $20.0\mu A$, including the raw (unfiltered) sinogram, reconstructed plume map and far-field plume sweep.

C. Nominal BET-300-P Current Ramp

Figure 11 summarizes CT reconstructions of measurement sets obtained during a sample current ramp over typical operating currents from a nominally configured BET-300-P operated at $100\mu A$ to $600\mu A$. These beam current set-points are typical of BET-300-P operation at up to 150 μN of thrust. Recall that for these measurements, and those in the following section, the physical design of the un-modified BET-300-P restricted the probe wire to a distance of $\sim 6 - 8mm$. Unlike above, the image intensity scale has been held fixed for all images within Fig. 11 to highlight variations in both the emission distribution and intensity. White lines indicate the notional locations of the nine emission edges integral to the thruster; although no clear correlation with the observed plume is evident. These data are noteworthy in that an increase in overall

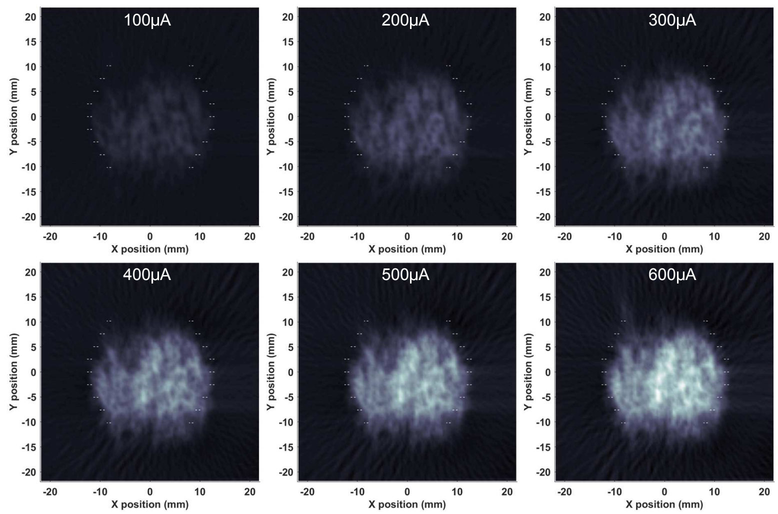

Figure 11. Reconstructed plume maps of obtained from a BET-300-P thruster operated at the indicated, increasing current levels. The image intensity scale is equal for all images.

intensity was observed yet clear variations in the emission distribution were less evident. Nevertheless some degree of emerging signal may be visible in the vicinity of the upper most emitter edge shown in the Figure. Here some new features were observed to form as the current increased, although the upper left quadrant of the thruster face was never observed to populate as densely as the central region.

The maximum probe current during these measurements was approximately 1.1% of the beam current during all measurements. The degree to which this constitutes an improvement over alternative mapping techniques, such as rastered probes is highly dependent on the specific apparatus used.

D. BET-300-P Beam Profiling over Long Durations

A primary motivation for developing the presented instrument has been to provide broad knowledge of emission localization over long durations when operating multiplexed source electrospray thrusters. One example of doing so is presented here, using the Busek BET-300-P operated over a ~ 200 hr period accumulating 31 Ns.

In Figure 12, sample images are provided after the indicated accumulated levels of impulse/throughput. Note that the beam current was typically between $250\mu A$ to $300\mu A$ during these measurements. In this test, the reconstructed plume initially indicated a broad distribution over the bulk of the thruster face. However, the concentration of emission shifted significantly over time; ultimately trending towards a largely bifurcated plume. As in the prior section, white lines indicate the notional emitter edge locations although correlation back to these source locations was again not clearly resolved by the measurement.

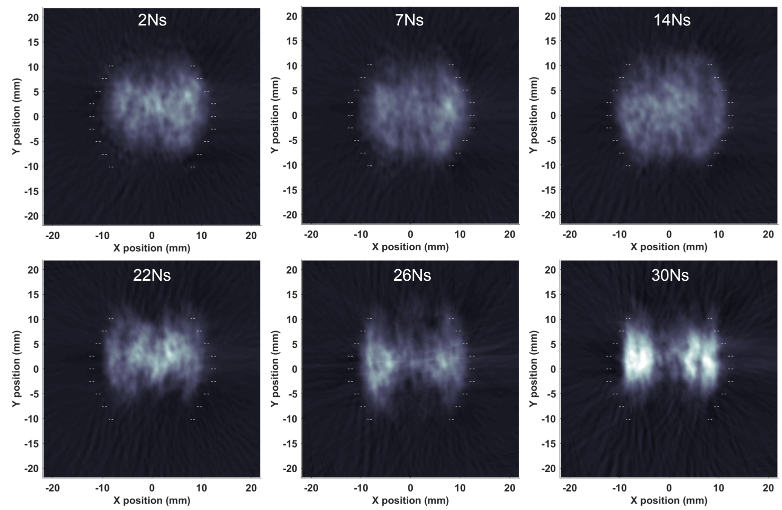

Figure 12. Reconstructed plume maps of obtained from a BET-300-P thruster operated over an extended period ($> 200hours$). The image intensity scale is equal for all images.

IV. Discussion

A primary goal of the work presented has been to validate if plume distributions reconstructed via computed tomography can provide useful insight into the characteristics of multiplexed electrospray sources. The reconstructions presented in section III.B indicate a few isolated concentrations of high current density. Far-field plume sweeps at low beam currents ($\leq 1\mu A$) also indicated discrete beamlets. Combined these observations support the notion that individual emission sites were localized via the CT reconstruction technique. However, the discrete emitter rows of the BET-300-P were not clearly resolved; as would have been expected based on the simulations shown in, for example, Fig. 6(b).

Simulations presented in section II.C assumed axial emissions for all sites; however, the centres of discrete beamlets captured with the far-field Faraday cup spanned at least 15^o with respect to vertical. These data were obtained when rotating the Faraday cup about an axis perpendicular to the emitter rows. Nevertheless, it may be reasonable to assume that -at a minimum- a similar level of beamlet direction variation may occur about an axis parallel to the emitter rows. The pitch between emitter rows on the BET-300-P is 2.54 mm. Meanwhile, a beam emitted at 15^o with respect to vertical would be displaced with respect to the emitter edge location by $1.0mm$ at $Z_{probe} = 4mm$; comparable to half of the emitter pitch. Accordingly, off-axis emission could significantly alter the degree to which emission may be localized to specific emitter edges on the BET-300-P. To exemplify consequences of this issue, Figure 13 presents simulated data obtained using the same emission sites shown in Fig. 3(a) yet with a variable emission angle tilted about an axis parallel to the emitter edges. Specifically, a random emission angle between $+15^o$ and -15^o was generated for each site. The theoretical Z_{probe} was set to $2mm$ in 13(a) and 4 mm in Fig. 13(b). The Figures show both the ideal/calculated plumes and those obtained via simulated CT experiments using $N_\phi = 60$ and $N_r = 121$.

Referring to Fig. 13(b) clear localization of emitter edges is no longer trivial when a distributed beamlet vector angle is assumed. Hence the poorly defined emitter rows in the images presented in Figs. 9 and 10 may be consistent with variations in the emitted beamlet angle. In addition to further far-field probing about both axes, this notion could, for example, be verified via three dimensional CT imaging reconstructed from multiple measurements at controlled Z_{probe} locations. Note that off-axis emissions were also reported in Ref. [10] when utilizing a rastered probe to map a passive electrospray source.

Variations in beam direction by 15^o (or higher) could be considered a significant compromise to performance; through increasing the probability of beam impingement on the extraction electrodes.[19] However, as illustrated in Fig. 9 each beamlet is observed to be relatively narrow; with a half-angle based on a Guassian fit of less than 5^o for all discrete peaks observed. Although these far-field measurements cannot be assumed to have intersected any one beamlet squarely through it's vertical axis of symmetry, such narrow plumes are not wholly inconsistent with previously reported plume shapes from individual electrospray emitters

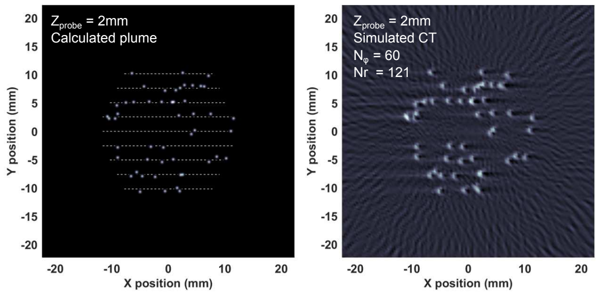

(a) $Z_{probe} = 2mm$

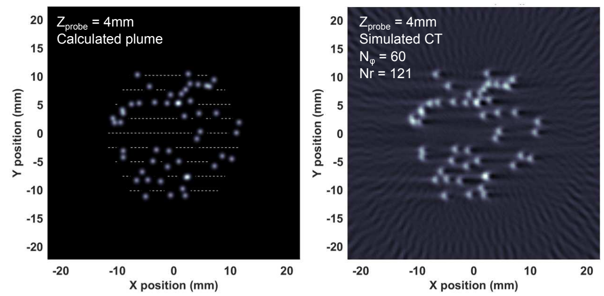

(b) $Z_{probe} = 4mm$

Figure 13. Simulated plumes from the same 50 emission site locations depicted in Fig. 3(a) each with a random emission angle with respect to horizontal uniformly sampled between $+15^o$ and -15^o.

operated in a highly ionic regime. If fit to a Gaussian profile, the data in Ref. [20] are approximated by a ~ 9 degree standard deviation. However, far-field visualizations in Ref. [21] appeared to indicate a much more narrow plume with no signal displayed at $<\sim 7.5^o$. As described in the description of Figs. 9 and 10 above, an evolving aggregate plume shape trending towards a single relatively centrally located plume with a half-angle of $\sim 9^o$ was observed as the number of active emission sites increases. This half-angle is consistent with the $7 - 9^o$ half-angle based on the width of a Gaussian fit ($2\sigma = 14 - 18^o$ for 95% of the current) typically observed from the BET-300-P about the same rotation axis. Again, three dimensional measurements with variable Z_{probe} could -if combined with enhancements to the CT instrument to improve physical stability- enable individual plume profiles to be mapped directly from the CT reconstruction.

It is important to reinforce that the axis of rotation for all far-field data presented was perpendicular to the emitter row spacing. Data from similar thrusters in Ref. [4] indicated an increase in plume width about the parallel axis when compared with perpendicular rotations. Similar plume data from the BET-300-P are therefore required to more accurately inform simulations and assess beam impingement risks.

The notion of narrow beamlets with varied direction provides insight into the make-up of multiplexed thruster plumes and suggests that their treatment in modelling of plume-to-grid interactions and other phenomena be carefully considered. Varied beamlet angles would also influence the interpretation of other far-field measurements such as beam spectra. In Ref. [4] a broad distribution of beamlet directions was highlighted as a possible contributor to observed irresolvable dependence of spectral distribution over beam angle. These factors clearly reinforce that complete multiplexed-source thrusters are not ideal platforms for scientific investigations into beamlet physics. However, significant variations in propellant feed conditions, geometry and other factors may greatly compromise the fidelity of results obtained using sources designed to yield single emission sites when viewed in the context of multiplexed sources.

Full-thruster data presented in sections III.B and D also indicated a poor level of emitter edge resolution. However; at an estimated Z_{probe} of 6 to $8mm$ this result is again consistent with variations in beamlet emission angle. In Fig.14 simulated plumes and CT reconstructions are presented with 300 emission sites randomly distributed over the BET-300-P face. Although emitters are reasonably resolved at $Z_{probe} = 2mm$, at $Z_{probe} = 8mm$ the plumes are merged to such a degree where only broad variations in emission localization can be resolved. Nevertheless, the presented experimental results illustrate that sufficient resolution remains at such large Z_{probe} locations to yield informative data. For example, in Fig. 11 relatively little emission was present in the upper left corner of the thruster face as emission was ramped up to $600\mu A$. Meanwhile, in Fig. 12, a clear variation in emission localization and concentration was demonstrated over $30Ns$ of throughput. Subsequent investigation into the drivers behind this localization have contributed to improving the throughput of the BET-300-P. Recent tests[22] have yielded over $70Ns$ of total impulse over > 350 hours and with a reduced degree of variation in plume localization over the course of testing.

The preliminary data presented provide additional insights into subtleties associated with BET-300-P operation. In particular, the distribution of current per emission site is currently poorly understood yet paramount to accurate modelling and performance analysis of thrusters like the BET-300-P. For example, Fig. 9(b) indicates approximately 14 to 20 emission sites were observed at $1\mu A$. Thus the average current per emission site was $\sim 50 - 70nA$. Additional data in section III.B clearly indicated an increase in the number of emission sites as current was ramped from $< 1\mu A$ through to $20\mu A$. However, ramping the current from a

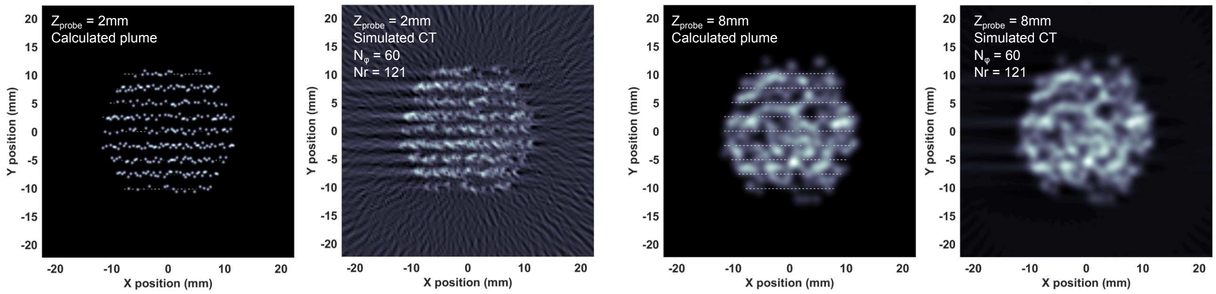

(a) $Z_{probe} = 2mm$ (b) $Z_{probe} = 8mm$

Figure 14. Simulated plumes from 300 emission site locations with a random emission angle with respect to horizontal uniformly sampled between $+15^o$ and -15^o.

different BET-300-P from $100\mu A$ to $600\mu A$ in Fig. 11 tended to indicate a combination of increased intensity along with some variation in the spatial distribution. Future work, leveraging the presented CT technique, is planned to further investigate the relationship between emission site number and intensity as contributors to net changes in beam current. These investigations may also extend into the dynamics of emission onset, where recent work[23] has indicated that variations in emission site onset time may also contribute to transient rates in aggregate beam current.

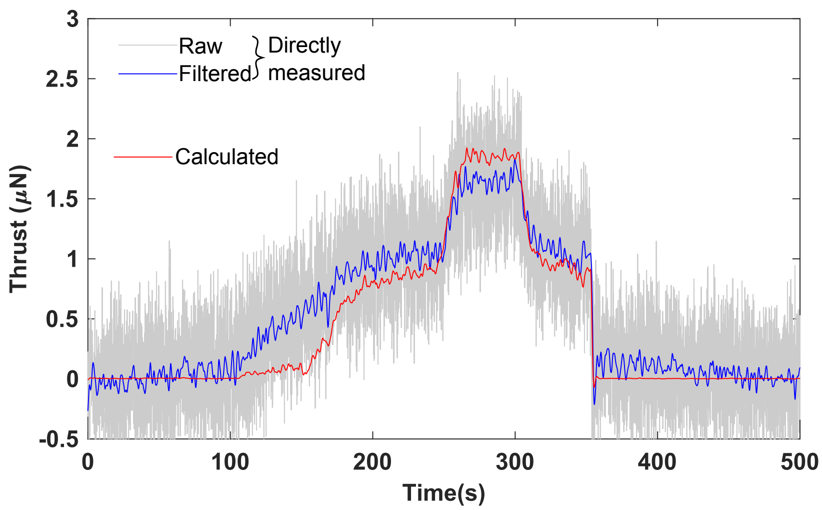

Figure 15. The BET-300-P calculated and directly measured thrust output when slowly ramping from an off-condition to low (μN scale) thrust levels.

Despite the intensity versus emission site count ambiguity, these results aid in the interpretation of recently obtained measurements of the minimum BET-300-P thrust. Sample data provided in Figure 15 demonstrate a controllable thrust level slowly ramped to approximately $1\mu N$, at which point the net beam current was 6 μA. The Figure summarizes both a calculated thrust level based on parameterized fits to direct measurements and the instantaneous direct thrust measurement made using Busek's torsional thrust stand.[24] The superposition of nearby plumes observed in the presented work did not permit reasonable estimates of the number of active emission sites above a few micro-amperes. However, given that up to 20 emission sites were operating at only $1.0\mu A$ in Fig. 9(b) and approximately half that number at $0.4\mu A$, it may be reasonable to infer that many 10's of emission sites were operational at $6\mu A$. Accordingly, discrete variations in thrust due to new emission site onsets may have comprised a small and sufficiently tolerable magnitude to maintain a high degree of control resolution at sub-micronewton thrust levels. Similarly, Busek has estimated calculated thrust noise at largely $< 0.1\mu N/Hz^{1/2}$ using the BET-300-P over a wide bandwidth from 10's of mHz to kHz levels.[23] Again, this capability may be -at least in part- achieved due to the relatively small contributions from each of many emission sites. This behaviour can be contrasted with that expected using Busek's Colloid Micro-Newton Thrusters flown aboard the ESA LISA Pathfinder mission.[25] With only 9 emitters on the CMNT each supporting a single Taylor cone, disturbances due to discrete activation or deactivation of individual emitters would yield a 1/9 (11%) variation in output if each emitter provides an equal intensity.

V. Conclusion

Asymmetric computed tomography has been used to reconstruct electrospray thruster current density maps using a custom-made instrument. Measurements of a BET-300-P passively fed electrospray thruster operated at low (μA scale) currents indicated a number of discrete current concentrations shown to increase concomitantly with the total beam current. Far-field plume measurements made at the same current set-points also indicated discrete current concentrations at low currents ($\leq 1\mu A$). These observations may be consistent with observations of individual emission sites and the distributed far-field plumes provide insight into the conditions inherent to passively fed electrospray sources. Specifically, the far-field plume was shown to trend towards a single roughly axially-aligned distribution as the number of emission sites increased. The data presented here reinforce the notion that the properties (e.g. width/shape) of this aggregate plume may not be representative of each emission site on the thruster. This result may therefore inform future efforts to accurately model passively fed thruster plumes and their interaction with extraction/acceleration electrodes.

Reconstructed plume maps obtained when operating BET-300-P thrusters at higher currents (100's of μA) indicated a variable degree of broad uniformity over the thruster face. In one sample instance, the plume distribution was shown to vary to only a limited degree when ramping the beam current from $100\mu A$ to $600\mu A$. Another example demonstrated a clear bifurcation of the plume distribution over the course of a high throughput ($31Ns$) test of the BET-300-P. The latter investigation has been used to inform subsequent upgrades to the BET-300-P which have contributed to more recent throughput tests exceeding $70Ns$ of total impulse. Although these measurements did not indicate absolute uniformity over the thruster face, the results exemplify the utility of the presented instrument and technique. That is, with this new information and capability in hand, both the means to improve uniformity and the efficacy of associated changes may be more rigorously pursued.

The nine linear emitter edges characteristic of the BET-300-P were not clearly resolved at any current set-point. The distributed far-field plume data obtained were used to motivate revised plume reconstruction simulations including a randomized beamlet direction. These simulations confirmed that at even a $4mm$ probe wire to source normal distance, clear resolution of the emitter edges may not be feasible. An issue further exacerbated at larger probe to emitter distances. Accordingly, future efforts seeking to identify and characterize individual emission sites will require a significantly reduced gap to the probe.

Efforts to probe in closer proximity to the emission sites may more rigorously inform estimates of the number of emission sites active as a function of beam current and their relative spacing versus operating points. Although limited, preliminary estimates of 10's of active sites at μA scale currents have provided new insight into interpreting low-thrust measurements including control authority well below $1\mu N$ along with thrust-noise measurements indicating noise levels below $0.1\mu N/Hz^{1/2}$

Further work is required to improve both the instrument and the analysis methodology. Slop within the linear position stage may have contributed to an inconsistent level of position knowledge variability depending on the scan direction and measurement angle. Quantitative assessments and optimizations of the reconstruction algorithm are required in order to generate a clear estimate of the measurement error and detailed limitations. At high beam currents ($> 100\mu A$), the scanning probe wire detected as much as 1.1% of the emitted plume. While a low level, a thinner probe wire may therefore continue to provide a trivially measurable signal using commercial picoammeters while further reducing interaction with the plume.

Acknowledgments

This work has been supported through a National Aeronautics and Space Administration Small Business Innovation and Research contract #80NSSC18C0052 monitored by Khary Parker of Goddard Space Flight Center. The authors would like to thank Nereo Alvarez and Nathaniel Demmons for their assistance.

References

[1]Gassend, B., Velasquez-Garcia, L. G., M., A. I. A., and Martinez-Sanchez, "A microfabricated planar electrospray array ionic liquid ion source with integrated extractor," *Microelectromechanical Systems, Journal of*, Vol. 18, No. 3, 2009, pp. 679–694.

[2]Dandavino, S., Ataman, C., Ryan, C. N., Chakraborty, S., Courtney, D. G., Stark, J. P. W., and Shea, H., "Microfabricated electrospray emitter arrays with integrated extractor and accelerator electrodes for the propulsion of small spacecraft," *Joanal of Micromechanics and Microengineering*, Vol. 24, No. 7, 2014, pp. 075011.

[3]Mier-Hicks, F. and Lozano, P. C., "Spacecraft-Charging Characteristics Induced by the Operation of Electrospray Thrusters," *Journal of Propulsion and Power*, 2016.

[4]Courtney, D. G., Dandavino, S., and Shea, H., "Comparing Direct and Indirect Thrust Measurements from Passively Fed Ionic Electrospray Thrusters," *Journal of Propulsion and Power*, Vol. 32, No. 2, 2015, pp. 392–407.

[5]Ziemer, J. K., Randolph, T. M., Franklin, G. W., Hruby, V., Spence, D., Demmons, N., Roy, T., Ehrbar, E., Zwahlen, J., Martin, R., and Connolly, W., "Colloid micro-newton thrusters for the space technology 7 mission," *IEEE Aerospace Conference 2010*, Big Sky, MT, March 2010, also AERO–2010–5446760.

[6]Tajmar, M., Vasiljevich, I., and Grienauer, W., "High current liquid metal ion source using porous tungsten multiemitters," *Ultramicroscopy*, Vol. 111, No. 1, 2010, pp. 1–4.

[7]Thuppul, A., Wright, P., and Wirz, R. E., "Lifetime Considerations and Estimation for Electrospray Thrusters," *2018 Joint Propulsion Conference*, Cincinnati, Ohio, July 2018, AIAA-2019-4652.

[8]Gassend, B., "A Fully Microfabricated Two-Dimensional Electrospray Array with Applications to Space Propulsion," PhD Thesis, Massachusetts Institute of Technology, Cambridge, MA, 2007.

[9]Courtney, D. G., "Ionic Liquid Ion Source Emitter Arrays Fabricated on Bulk Porous Substrates for Spacecraft Propulsion," Ph.D Thesis, Massachusetts Institute of Technology, Cambridge, MA, 2011.

[10]Guerra-Garcia, C., Krejci, D., and Lozano, P., "Spatial uniformity of the current emitted by an array of passively fed electrospray porous emitters," *Journal of Physics D: Applied Physics*, Vol. 49, No. 11, 2016, pp. 115503.

[11]Monnig, C., Gebhart, B., Marshall, K., and Hieftje, G., "Tomographic image reconstruction techniques for spectroscopic," *Spectrochimica Acta Part B: Atomic Spectroscopy*, Vol. 45, No. 3, 1990, pp. 261–270.

[12]Zhang, F.-Y., Fujiwara, T., and Komurasaki, K., "Diode-laser tomography for arcjet plume reconstruction," *Applied optics*, Vol. 40, No. 6, 2001, pp. 957–964.

[13]Rathore, K., Bhattacharjee, S., Patel, D. N., and Munshi, P., "Optical Emission Spectroscopy-Based Tomography for Compact Low-Pressure Microwave Plasma in a Multicusp," *IEEE Transactions on Plasma Science*, Vol. 45, No. 9, 2017, pp. 2492–2503.

[14]Landes, K., Forster, G., Zierhut, J., Dzulko, M., and Hawley, D., "Computer tomography of plasma jets–applied on a TRIPLEX II torch," *Proceedings of the International Thermal Spray Conference*, 2004.

[15]Matlock, T., Hargus, W., Larson, C., and Nakles, M., "Inversion Method for Reconstructing Hall Thruster Plume Parameters from Optical Measurements," *43rd AIAA/ASME/SAE/ASEE Joint Propulsion Conference & Exhibit*, AIAA-2007-5303.

[16]Fessler, J., "Image Reconstruction: Algorithms and Analysis," Bookdraft, downloaded Aug. 2018.

[17]Kak, A. C., Slaney, M., and Wang, G., "Principles of computerized tomographic imaging," *Medical Physics*, Vol. 29, No. 1, 2002, pp. 107–107.

[18]Courtney, D. G., Alvarez, N., and Demmons, N. R., "Electrospray Thrusters for Small Spacecraft Control: Pulsed and Steady State Operation," *2018 Joint Propulsion Conference*, Cincinnati, OH, July 2018, AIAA-2018-4654.

[19]Wright, P., Thuppul, A., and Wirz, R. E., "Life-Limiting Emission Modes for Electrospray Thrusters," *2018 AIAA Joint Propulsion Conference*, Cincinnati, OH, July 2018, AIAA-2018-4726.

[20]Lozano, P. and Martínez-Sánchez, M., "Ionic liquid ion sources: characterization of externally wetted emitters," *Journal of Colloid and Interface Sciences*, Vol. 282, No. 2, 2005, pp. 415.

[21]Perez-Martinez, C. S. and Lozano, P. C., "Visualization of beams from ionic liquid ion sources for focused ion beam applications," *Journal of Vacuum Science & Technology B, Nanotechnology and Microelectronics: Materials, Processing, Measurement, and Phenomena*, Vol. 30, No. 6, 2012, pp. 06F601.

[22]Courtney, D. G., Wood, Z., and Fedkiw, T., "Electrospray Propulsion Direct Thrust Characteristic Changes Over Extended Impulse," *Article in Preparaton for the AIAA Journal of Propulsion and Power*, 2019.

[23]Courtney, D. G., Wood, Z., Model, J., and Gray, S., "High-Speed Transient Characterization of the Busek BET-300-P Electrospray Thruster," *The 36th International Electric Propulsion Conference*, Vienna, Austria, September 2019, IEPC-2019-788.

[24]Gamero-Castaño, M., Hruby, V., and Martínez-Sánchez, M., "A torsional balance that resolves sub-micro-Newton forces," *27th International Electric Propulsion Conference*, Pasadena, CA, 2001.

[25]Ziemer, J., Marrese-Reading, C., Dunn, C., Romero-Wolf, A., Cutler, C., Javidnia, S., Li, T., Li, I., Franklin, G., Barela, P., et al., "Colloid Microthruster Flight Performance Results from Space Technology 7 Disturbance Reduction System," 35th *International Elecric Propulsion Conference*, Atlanta, GA, October 2017, also IEPC-2017-578.